Integration of Optimized Leading Edge Geometries Onto Waverider Configurations

Dr. Patrick E. Rodi[1]

Lockheed Martin Corporation, Houston, TX

Most popular waverider design approaches produce vehicles that have sharp leading edges. Manufacturing and/or thermal limits require that some degree of finite radius be employed at the leading edge. Earlier research has produced an optimized leading edge generation process suitable for high speed vehicles such as waveriders. In that effort, Bezier Curves were employed to represent the candidate leading edge cross sectional geometries which were then optimized using a number of cost functions including: minimum peak heating, minimum total heating, minimum drag, and minimum pressure gradient.

In the current work, Bezier Curve leading edges have been optimized to reduce the peak leading edge laminar heating for use on waverider-based vehicles designed for three typical hypersonic applications: a Mach 5 Air-Breathing Missile, a Mach 10 Hypersonic Cruise Vehicle, and a Mach 20 Boost-Glide Vehicle. These leading edge geometries have been incorporated onto the vehicles and the resulting integrated aerodynamic performance has been quantified and compared to similar vehicles with conventional hemi-cylindrical leading edge configurations. The largest drag reduction was for the Mach 5 missile, where a 6.2% reduction was predicted when using optimized leading edges on both the inlet and fins.

Nomenclature

h	= altitude
n	= power law body exponent
q	= local convective heating rate
qbar	= freestream dynamic pressure
r	= power law body local radius
r_b	= power law body base radius
r_{CL}	= leading edge centerline radius
r_{swept}	= radius for a swept leading edge
t	= independent parameter in the Bezier Curve equation
C_p	= pressure coefficient
D	= drag
L	= lift, streamwise length of waverider on a given osculating plane
M	= freestream Mach number
X	= streamwise distance from the waverider's nose, also streamwise distance on a leading edge
Y	= spanwise distance from the centerline of the waverider, also vertical distance on a leading edge
Z	= vertical distance on the waverider measured from a waterline datum
θ	= leading edge wedge angle
θ_c	= cone angle of power law body on the osculating plane
λ_{loc}	= local leading edge sweep angle
φ	= leading edge position angle, measured from the most forward point on a leading edge

I. Introduction

THE pursuit of high lift-to-drag ratio (L/D) supersonic/hypersonic vehicles has been underway for decades. By taking advantage of the hyperbolic nature of the inviscid flowfield, vehicle performance can be greatly increased. One such utilization of this approach is the waverider family of vehicles. Waveriders effectively increase the lift generated from a vehicle moving through the air, at Mach numbers greater than unity, by riding the shock wave that the vehicle itself has created.

---

[1]Lockheed Martin Fellow, AIAA Associate Fellow

Various waverider approaches have been developed since the 1950's[1, 2]. The earliest designs were based on two-dimensional wedge flowfields. Such waveriders are called Caret Waveriders, due to their shape. An example of a Caret Waverider is shown in Figure 1. For axisymmetric shock wave shapes, the Conical Method (CM) has been extensively developed[3, 4]. However, limits to vehicle L/D ratios exist with the conical approach. In order to further increase the L/D of waveriders at useful lift coefficients, the Osculating Cones Method (OCM) was developed. This approach permits a more general definition of the possible shock wave shapes and a significant improvement in waverider L/D was obtained[5-7]. The generalization of the Osculating Cones Method is the Osculating Flowfield Method[8] (OFM), currently using a series of "power law body"-based flowfields are employed on each osculating plane. Wedge-based methods, and both the CM and the OCM are subsets of the OFM. The OFM produces vehicles with modestly improved L/D performance over those from the OCM[9], while increasing design flexibility.

In both the OCM and OFM, the procedure used to generate the waverider geometry begins by prescribing the upper surface trace and the shock wave trace on the baseplane of the waverider vehicle. The baseplane of an Osculating Waverider is illustrated in Figure 2, from Reference 10. The zero radius (i.e. sharp) leading edge of the waverider is then found by determining the intersection point between each osculating plane and the upper surface, at the shock angle generated by the local flowfield on that osculating plane. With the leading edge defined, the waverider lower surface can be created by tracing streamlines from the leading edge point within each osculating plane.

In the Osculating Flowfield Method a series of known flowfields, such as those produced by a "power law body," are employed on each osculating plane. For power law bodies the local body radius, r, is a function of position along the body defined by,

$$\frac{r}{r_b} = \left(\frac{X}{L}\right)^n$$

where r_b is the radius of the power law body at the base of the body, X is the vehicle axis measured from the nose and moving towards the base, L is the total body length, n is the exponent in the power law body expression. Typically, the exponent varies between $0.75 \leq n \leq 1.1$. (Note that a cone is produced when n equals unity.) A power law body-based flowfield was selected for use on the osculating planes in the new method due to the pressure drag reduction observed in power law bodies when compared to cones[1]. Much of this drag reduction benefit can now be incorporated into waveriders. On each osculating plane, shown in side view in Figure 3, the waverider is generated with a sharp leading edge (shown in black). The upper surface of the waverider is aligned with the freestream flow direction. The lower surface is defined by tracing the flowfield produced by the assumed geometry such as that generated by a power-law body. The wedge angle, θ, is the lower surface local angle measured from the freestream direction at the downstream edge of the leading edge.

One outstanding question regarding the performance of waverider shapes is the concern that the predicted performance of such shapes with infinitely sharp leading edges will not be achieved when finite radius leading edges are included. Due to manufacturability and/or aeroheating concerns, a truly sharp leading edge is not possible. This limitation exists for waveriders and any other high speed vehicle design approach that calls for sharp leading edges. Waveriders depend on leading edge shock attachment to their forward surface in order to contain the high pressure air that produces efficient lift, and are particularly vulnerable to the impacts from finite leading edges. General studies of what constitutes aerodynamically "sharp" vs. "blunt" leading edge geometries for high speed vehicles have been conducted[11]. Specific to waverider-based vehicle configurations, the impacts from hemi-cylindrical and power-law body leading edges on performance have been examined[12-16]. O'Brien and Lewis[13] employed power-law curve finite leading edge geometries and showed blunt body-like pressure gradient behavior very close to the stagnation point. Vanmol and Anderson[16] examined the heat transfer to hypersonic waveriders, with an emphasis on effects caused by the finite leading edge. They incorporated a hemi-cylindrical leading edge blunting technique, with the local leading edge radius as a function of spanwise position.

In an effort to develop finite leading edge geometries with superior aerodynamic and/or aerothermodynamic performance, an evaluation of using Bezier Curves to create leading edge geometries for high speed vehicles was performed[17]. This earlier work demonstrated that Bezier Curve-based geometries could be optimized to offer advantages over previously employed leading edge geometry approaches such as hemi-cylindrical or power-law curve based designs. Third- through sixth-order Bezier Curve-based leading edges were generated and their performance optimized using a number of criteria including; pressure drag, surface pressure gradient, stagnation

2

American Institute of Aeronautics and Astronautics

point heating, and laminar and turbulent acreage heating. A Genetic Algorithm (GA) optimization process was used to perform the optimization by physically relocating the control points used to define the Bezier Curve.

Leading edge geometry optimizations were conducted using the "cold wall" (100º F) acreage convective heating distribution assuming either laminar flow or turbulent flow was used as the cost function. In these cases the peak value in convective heating was minimized. The goal was to reduce the convective heating around the stagnation point, while increasing the convective heating away from the stagnation point region, to better utilize a given leading edge material's thermal limits. No contributions from of other heating mechanisms (e.g. shock layer radiation) are included. The resulting cases are significantly blunter than a corresponding hemi-cylindrical leading edge. For freestream conditions of Mach=10 and dynamic pressure, qbar, of 2000psf, peak heating was reduced by 23.4% and 28.2% in the laminar and turbulent cases, respectively, for leading edges with a nominal radius of ½ inch. This heating reduction was obtained by blunting the leading edge around the stagnation region. This blunting increased the pressure drag by 17.4% and 16.8% for the two boundary layer state assumptions. Similar CFD-based optimizations have produced qualitatively similar geometries for different conditions[18]. A reduction in the physical scale of the leading edge has been offered as one method to reduce the drag. For the Mach 10 laminar case, qualitative analysis[19] has predicted that optimized Bezier Curve leading edges will produce a 1.7-13% reduction in inviscid pressure drag over hemi-cylindrical leading edges at the same magnitude of peak convective laminar heating corresponding to a maximum radiative equilibrium temperature of 3500ºF.

In this paper, optimized Bezier Curve Leading Edges (BCLE) will be generated for waverider-based vehicles designed for three typical hypersonic missions. These leading edges will then be integrated on the waveriders and the resulting vehicle-level aerodynamic impacts and aerothermodynamic performance will be quantified. The results will be discussed for the three specific hypersonic waveriders at design conditions, with trends identified from supplemental solutions. In the author's earlier work[17,19], a Genetic Algorithm optimization process was used to perform the optimization by physically relocating the control points used to define the Bezier Curve. For the current study, the GA–based process has been replaced with a Particle Swarm Optimization (PSO)[20] process to perform the optimizations in Matlab using a PSO toolbox[21] from the user community. For this application and at these conditions, the PSO approach outperformed the GA approach in both speed and optimum answer quality.

II. Employing Bezier Curves as Leading Edge Geometries

Employing Bezier Curves is a versatile method for using a small number of input variables to generate geometries that are continuous and differentiable. Consequently, these attributes make them attractive for use in aerospace optimization problems[22-24]. The Bezier Curve is a particular linear combination of the (X, Y) control point pairings re-parameterized via the independent variable, t. Using control points CP1, CP2, CP3, CP4, and CP5, a fourth order Bezier Curve is defined by,

$$P(t) = J41(t)*CP1 + J42(t)*CP2 + J43(t)*CP3 + J44(t)*CP4 + J45(t)*CP5, \text{ for } 0<=t<=1$$

with the Bernstein polynomials,

$$J41(t) = (1-t)^4 = 1 \ (1-t)^4 * t^0$$
$$J42(t) = 4 \ (1-t)^3 * t = 4 \ (1-t)^3 * t^1$$
$$J43(t) = 6 \ (1-t)^2 * t^2 = 6 \ (1-t)^2 * t^2$$
$$J44(t) = 4 \ (1-t) * t^3 = 4 \ (1-t)^1 * t^3$$
$$J45(t) = t^4 = 1 \ (1-t)^0 * t^4$$

Lower and higher order Bezier Curves are possible. Up to sixth order curves have been examined for this BCLE optimization application, but these formulations did not provide superior results to those from fourth order curves and often lead to convergence problems[17]. Consequently, this paper will present results from optimizations performed using only fourth order Bezier Curves.

An example of a leading edge generated by a fourth order Bezier Curve is shown in Figure 4. In this figure the flow is assumed to be moving from the left towards the right. This Bezier Curve is modeled by 101 points (100 facets), illustrated by a blue line. The five control points are located by red "+" symbols and connected by a red line, and are labeled CP1-CP5. The bottom of the leading edge (at point X=10, Y=0) is tangential with the windward surface of the waverider. In this example, the windward surface has a local compression angle of eight degrees at the leading edge tangent point on this osculating plane. The top of the leading edge (at point X=10, Y=1) is tangential with a horizontal line representing the waverider upper surface on this osculating plane. The first control point is at

(10, 0), the beginning of the leading edge. The second control point at (9.738, 0.035) is located along on a line angled at eight degrees to the X-axis to generate the tangency of the Bezier Curve with the waverider lower surface. The third control point is at (9.156, 0.515) which was selected by the optimizer for this problem. The fourth control point at (9.779, 1) is along a horizontal line at Y=1 to generate tangency between the Bezier Curve and the horizontal waverider upper surface. The fifth and final control point is at (10, 1), the tangent point between the leading edge and the upper surface. The adjacent waverider upper and lower surfaces are represented by the two straight blue lines to the right of the leading edge. This particular BCLE is quite symmetrical from top-to-bottom. A simple hemi-cylindrical leading edge (HCLE) is shown in green for reference. In this example, the Bezier Curve leading edge is less bulbous (i.e. enclosing less cross sectional area) than the HCLE.

The research reported in Reference 19 was focused on exploiting a given leading edge Thermal Protection System (TPS) material to its maximum potential by shaping the leading edge to more evenly distribute the heating. Consequently, more of the TPS will be working at its maximum temperature than with other leading edge geometries such as a HCLE. Bezier Curves were employed to prescribe the candidate leading edges, and a Genetic Algorithm was used to perform an optimization to reduce the peak laminar heating rate on the leading edge. This laminar convective heating was predicted using the correlation by Kays[25]. The optimized design process has produced leading edge configurations with a locally blunter geometry near the stagnation point and with shoulder features further away from the stagnation point.

For later comparisons, a characteristic length scale is required to describe the Bezier Curve leading edge size. Radius is not appropriate as the local radius varies around the BCLEs. The distance measured, within a given osculating plane, from the first control point (CP1) to the fifth control point (CP5) has been employed and is identified as the "Total Height." This parameter will be used to quantify the scaling performed to the leading edges and in the calculation of the leading edge Reynolds number.

III. Hypersonic Vehicles

Three typical hypersonic missions were defined for waverider-based vehicle designs and subsequent optimized Bezier Curve Leading Edge integration. These three are: 1) Mach 5 Hydrocarbon-fueled Air-Breathing Missile (ABM), 2) Mach 10 Hydrocarbon-fueled Air-Breathing Hypersonic Cruise Vehicle (HCV), and a 3) Mach 20 Boost-Glide Vehicle (BGV). For each of these three missions, a representative osculating flowfield waverider-based vehicle was designed. Bezier Curve Leading Edges were then defined for each of the flight conditions and the peak heating rates quantified. These BCLE were scaled to account for leading edge sweep angle, and integrated onto the waveriders and the vehicle-level aerodynamic impacts quantified.

A. Air-Breathing Missile

The first mission/waverider to be discussed is that of a short range hypersonic missile configuration using a hydrocarbon-fueled scramjet propulsion system. The prototype for such a vehicle is the DARPA/Boeing X-51A. An artist's interpretation of the X-51A flying while still attached to its solid-fueled booster is shown in Figure 5. This vehicle is of modest size, with a total body length of approximately 14 feet. For this case the design freestream conditions were defined as Mach=5 at h=70,000 ft. altitude. This represents a typical flight environment for the X-51A[26]. The ABM's Reynolds number based on total body length and freestream conditions is 31.3×10^6.

The ABM waverider forebody was designed as a simple two-dimensional wedge with a flat compression surface angled at 10º to the freestream flow. The shock wave trace was a horizontal line at which a cowl was positioned to capture the shock wave. This cowl was extended up both sides of the vehicle and became the OML for those regions. A constant cross sectional extension and aft body close-out were added to generate an internal flow geometry that approximates that of the X-51A and which produced the designed overall length of the vehicle to 14 feet. Four double-wedge fins were added, as in the X-51A configuration. (This number does not include the fins on the booster). Each of the fins has a root chord of 2.25 feet, with a taper ratio of 0.8, a height of 0.69 feet, a root thickness-to-chord ratio of 0.08, and tip thickness-to-chord ratio of 0.05. These were sized to approximate those on the X-51A. No stability and control assessment was conducted to evaluate the adequacy of these fixed control surfaces. The BCLE installation was initially conceived for the two-dimensional leading edge only. However, leading edge modifications were also made to the four fins. Consequently, the performance advantages quoted here are conservative as further improvements are possible by applying optimized geometries to any remaining leading edge regions, such as the cowl.

The final Mach 5 ABM configuration is shown in Figure 6. The aerodynamic surfaces were defined as the inlet, the Outer Mold Line (OML) of the forebody, the OML of the cowl, and the fins. The forces on the interior surfaces and on the nozzle area are bookkept under propulsion. The force accounting system[27] employed for this vehicle and

American Institute of Aeronautics and Astronautics

for the Mach 10 Hypersonic Cruise Vehicle is shown in Figure 7. For the Mach 5 ABM the nozzle area does not extend beyond the propulsion system enclosure.

B. Hypersonic Cruise Vehicle

The second mission/waverider is that of a large Hypersonic Cruise Vehicle. Such a vehicle would spend extensive periods of time at hypersonic cruise conditions, most likely using a hydrocarbon/hydrogen-fueled scramjet propulsion system. The prototype for such a vehicle is the DARPA Hypersonic Cruise Vehicle from the Falcon program. An artist's interpretation of a DARPA HCV is shown in Figure 8. Such vehicle designs are quite large, with a total body length on the order of 100 feet. For this case the freestream conditions were defined as Mach=10 at h=95,100 ft. altitude, which produces a freestream dynamic pressure of 2000psf. This is a typical condition for a scramjet powered vehicle[28]. Consequently, the HCV's length Reynolds number is 131.6×10^6.

An Osculating Flowfield Waverider was generated and used as the forebody of the HCV vehicle. The assumed shock wave trace (shown in blue) and the upper surface trace (shown in red) are shown in Figure 9. The waverider's n-factor and upper surface expansion angle distributions are shown in Figures 10 a) and 10 b), respectively. The n-factor begins with a convex shape (n>1) at the centerline of the vehicle where the spanwise value is identically zero. This portion of the waverider-based forebody functions as the inlet for the engine and a convex shape is more efficient for this propulsion-dominated region than a flat ramp geometry or a blunted shape. Outboard of this region, the n-factor passes through unity (i.e. locally an Osculating Cone waverider plane) around 30% of the semi-span, and then linearly drops to a value of 0.75 at the wing tip. A blunted shape, where the n-factor is less than one, is used in aerodynamic-dominated regions to improve lift-to-drag ratio performance. The upper surface expansion angle begins at 2° at the centerline and linearly increases to 4° at the wing tip. These values are typical for hypersonic waveriders. No attempt to optimize the n-factor, upper surface angle, cone angle distributions, or the shock wave or upper surface traces to these conditions; rather the Mach 10 HCV was designed to represent typical vehicle size and characteristics.

Two double-wedge fins were added, as illustrated in the final HCV configuration in Figure 11. Each of the fins has a root chord of 14 feet, with a taper ratio of 0.4, root thickness-to-chord ratio of 0.06 and tip thickness-to-chord ratio of 0.05. These values were chosen to approximate those on Hypersonic Cruise Vehicle configurations. No stability and control assessment was conducted to evaluate the adequacy of these fixed control surfaces. The optimized BCLE installation was initially used on the waverider forebody portion of the fuselage only. Later, modifications were also made to the two fins. As with the early ABM vehicle, the HCV performance advantages quoted herein are conservative as further improvements are possible by applying optimized geometries to these other leading edge regions. Also as before, the forces on the interior surfaces of the propulsion system and the nozzle region behind the engine were not calculated for this vehicle and do not appear in any aerodynamic performance quoted values or comparisons.

C. Boost-Glide Vehicle

The third and final mission is that of a high Mach number Boost-Glide Vehicle. Such a vehicle is propelled to great speed and altitude by a large booster, and then re-enters the atmosphere to begin a long hypersonic glide. The prototype example for such a vehicle is the DARPA Hypersonic Test Vehicle-2. An artist's rendering of the HTV-2 in flight is shown in Figure 12. Such vehicles are modest in size, with a total body length on the order of 12 feet. For this case the freestream conditions were defined as Mach=20 at h=120,000 ft. altitude. These conditions are representative for a gliding vehicle such as the HTV-2[29]. The vehicle's length Reynolds number is 9.44×10^6.

A waverider was designed for the BGV mission. This vehicle was closed by a flat base at the downstream end of the waverider, orientated normal to the freestream direction. This feature mimics the base geometry found on the DARPA HTV-2 vehicle. The shock wave trace (shown in blue) and the upper surface trace (shown in red) for the BGV are illustrated in Figure 13. The upper surface trace features a convex center region, relaxing to slightly concave geometry as the span is increased. This is comparable to the HTV-2 geometry. To better mimic the general arrangement of the HTV-2, the BGV waverider was terminated at 70% semi-span, as illustrated by the vertical black line. This choice was made somewhat arbitrarily to approximate the characteristics of the HTV-2. A constant cone angle of 10° was used, and n-factor and upper surface expansion angle of 0.75 and 2° were employed, respectively, to generate the waverider. The resulting vehicle is shown in Figure 14. No attempt was made to optimize these waverider variables for the mission. As for the HTV-2 configuration, no fins were installed. Therefore, the optimized BCLE installation was installed on the waverider forebody only.

American Institute of Aeronautics and Astronautics

IV. Results and Discussion

Optimized Bezier Curve Leading Edges were generated for the three sets of freestream conditions mentioned earlier, assuming a 1976 Standard Atmosphere. Initially, leading edges with a Total Height of 1" were generated. This value was chosen somewhat arbitrary, but was hoped to be a representative value for the waverider leading edge final dimensions. These optimizations were performed using a laminar flow, "cold wall" (100º F) acreage convective heating distribution within the cost function. As in the earlier work[17,19], the peak value in convective heating was minimized. No contributions from other heating mechanisms (e.g. shock layer radiation) were considered. The resulting leading edge geometries are significantly blunter than observed in a corresponding hemi-cylindrical leading edge. Similar CFD-based optimizations have produced qualitatively similar geometries for different conditions[18]. A reduction in the physical scale of the leading edge has been offered as one method to reduce the drag. As mention earlier, for a Mach 10 laminar case a qualitative analysis[19] has predicted that optimized Bezier Curve leading edges will have a 1.7-13% reduction in drag over hemi-cylindrical leading edges at the same magnitude of peak convective laminar heating corresponding to a maximum radiative equilibrium temperature of 3500ºF.

A. Nominal Two-Dimensional Results

An example BCLE geometry and laminar heating rate distribution is shown in Figures 15 and 16, respectively. This geometry was optimized using the freestream conditions of Mach 5 at 70,000 ft. altitude, with a Total Height of 1". In Figure 15 the optimized BCLE is represented by a blue curved line, while the five control points are marked by red "+" symbols and connected by a red line. For comparisons, a HCLE geometry is shown in green. As in earlier studies, the optimized geometry is blunter than the HCLE. The heating data are plotted in BTU/ft^{2}sec, using the ordinate φ as the angle of a given position along the leading edge measured from the most forward leading edge point (i.e. $\varphi \approx 0º$ at the flowfield stagnation point.) The BCLE is significantly blunter than the HCLE around the middle of the leading edge. This feature has been added by the optimizer to reduce the acreage heating around the stagnation point. To maintain the cross sectional area, the BCLE is pushed out beyond the HCLE geometry, generating one large "shoulder" feature near the top of the leading edge. The very top of the leading edge is aligned with the flat upper surface of the waverider on this osculating plane and the CP4 control point's vertical location ensures that the BCLE is tangent with this surface.

This optimization process was repeated for Mach 10 and 95,100 ft. altitude and Mach 20 at 120,000 ft. altitude conditions, again using a Total Height value of 1". The optimized Bezier Curve Leading Edges for these two vehicles are shown in Figure 17 and 18, respectively. As seen at Mach 5, the optimized leading edges are blunter than the HCLE and biased towards the flat upper surface. For all three vehicles, a unique optimization was not conducted on each osculating plane as the differences in physical characteristics between planes were insignificant. For the Mach 5 ABM and the Mach 20 BGV these differences were identically zero. For the Mach 10 HCV these differences were very small, and assumed to be inconsequential to the quantification of the vehicle-level aerodynamic impacts.

B. Reynolds Number Sensitivity

From the nominal Total Height value, a Reynolds number sensitivity was performed by optimizing BCLEs at Total Heights of 0.1" and 12" (1 foot) at each of the three Mach numbers, for a total of nine optimization runs. For these cases, the Reynolds number based on freestream conditions, using the Total Height as the length scale, is plotted against Mach number in Figure 19. The three Reynolds numbers at a given Mach number are connected by a colored line. Blue, black, and red lines were used to identify the freestream Mach numbers 5, 10, and 20, respectively.

For the three BCLE optimizations performed at Mach 5 and 70,000 ft. altitude, the three leading edges were very similar in shape. While the absolute heating rates varied considerably, the BCLE shape that generated the lowest peak value remained quite constant. These three leading edge shapes are compared in Figure 20. The Total Height values are differentiated by the line color, with blue, black, and red indicating the 0.1", 1", and 12" Total Heights, respectively. The similarity of the leading edge geometry indicates little sensitivity to Reynolds number over this two orders of magnitude variation in range. The three optimized leading edges generated at Mach 10 and 95,100 ft. altitude are shown in Figure 21. As for the Mach 5 conditions, nearly identical shapes over this Reynolds number range. This trend continued at Mach 20 and 120,000 ft. altitude, as shown in Figure 22. The insensitivity of optimized shape to Reynolds number permits application of the geometries generated for the nominal conditions to be successfully employed over a range of physical sizes. This engineering assumption will avoid re-optimization of

American Institute of Aeronautics and Astronautics

the leading edges at every unique size within the range of interest.

While the optimized shapes showed little variation over a significant range in Reynolds number, the Mach number sensitivity was slightly more apparent. The three optimized BCLE geometries generated for the nominal conditions at the three Mach numbers, and using a Total Height of 1", are shown in Figure 23. Although small, a slight variation in shaping due to Mach number has been observed. This trend is consistent with the Mach number sensitivity reported in Reference 17. (It is important to highlight that the Mach 10 geometry uses a smaller wedge angle of 8.5º, versus 10º for the other two configurations. This difference has a subtle change in the shaping, especially near the bottom of the leading edge. In this region, the black line of the Mach 10 configuration can be seen to be lower than the other two configurations. This behavior is driven by the BCLE constraint to be tangent with the waverider's lower surface at the first control point.)

The vehicle implications for the BCLEs having virtually no Reynolds number sensitivity and only a very small sensitivity to Mach number is that such optimized leading edge shapes should generate a robust design and able to offer benefits over a range of conditions. However, the author must point out that sensitivities to angle-of-attack variation have neither been examined nor quantified.

C. Centerline Leading Edge Geometry Scaling

The radiative equilibrium temperature is the temperature at which the convective heat transfer into the surface is balanced by the radiative heat transfer away from the surface. No conduction into the vehicle is modeled. For many hypersonic vehicles, the surface temperature at the Thermal Protection System (TPS) design conditions is near the local radiative equilibrium temperature. As such this temperature is often used to define TPS material splitlines on the OML. Given freestream conditions and a cold wall heating rate, the radiative equilibrium temperature can be calculated. For this study the TPS surface emissivity was assumed to be 0.9, and the radiation sink temperature was defined as 0ºR. Figure 24 illustrates the relationship between radiative equilibrium temperature and cold wall heating rates for the three freestream conditions.

At each of the three Mach numbers, the Reynolds number insensitivity described earlier was used to justify the use of simple geometric scaling of the optimized BCLE produced at the nominal conditions to obtain BCLE geometries for various leading edge radiative equilibrium temperatures. In this process, the nominal BCLE was read in and parametrically scaled. The peak heating for each scaled geometry was then calculated and the radiative equilibrium temperature determined. The end result is an implicit relationship between peak radiative equilibrium temperature of the leading edge TPS material and the leading edge scale.

The peak temperature limit plotted against leading edge scaling, for the BCLE and the HCLE at Mach 5 and 70,000 ft. altitude, is shown in Figure 25 a) and 25 b), respectively. Therefore, assuming a given leading edge TPS material temperature limit of, say, 1400ºF, the BCLE could be scaled down to a Total Height of 1.45". In contrast, the HCLE can only be scaled down to 1.80" Total Height before reaching the material temperature limit. In this case, the pressure drag generated by the smaller BCLE is approximately 11.8% lower than that for the HCLE. Although the BCLE geometry is blunter, the lower heating permits a smaller scale to be employed which reduces the pressure drag generated by the leading edge. Later in this paper, the scaled BCLE and HCLE will be incorporated onto the ABM and the drag reduction impacts quantified at the vehicle level.

The peak temperature limit on the BCLE and a HCLE at Mach 10 and 95,100 ft. altitude, is shown in Figures 26 a) and 26 b), respectively. Assuming a given leading edge TPS material temperature limit of, 3500ºF, the BCLE could be scaled down to a Total Height of 1.95". By comparison, the HCLE can only be scaled down to 2.40" Total Height before reaching the material temperature limit. The pressure drag generated by the smaller BCLE is approximately 11.2% lower than that for the HCLE. As in the Mach 5 ABM example the BCLE geometry is blunter and the lower heating permits a smaller scale to be employed to reduce the pressure drag. Later in this paper, the scaled BCLE and HCLE will be incorporated onto the HCV and the pressure drag reduction impacts quantified at the vehicle level.

The peak temperature limit on the BCLE and a HCLE at Mach 20 and 120,000 ft. altitude, is shown in Figures 27 a) and 27 b), respectively. Assuming a given leading edge TPS material temperature limit of 6000ºF, the BCLE could be scaled down to a Total Height of 4.70". (This extremely high temperature value is potentially possible with advanced materials[30-33].) In contrast, the HCLE can be scaled down to 5.25" Total Height before reaching the material temperature limit. The pressure drag generated by the smaller BCLE is approximately 2.1% lower than that for the HCLE. In this example, the drag reduction advantages observed for the BCLE are reduced for the BGV. Later in this paper, the scaled BCLE and HCLE will be incorporated onto the BGV and the drag reduction impacts quantified at the vehicle level.

D. Off-Centerline Scaling

The three optimized BCLEs discussed above represent geometries for use on the unswept portions of the leading, such as at the waverider's vehicle centerline. With these optimized BCLEs defined, integrations onto the mission specific waveriders could begin. Both the optimized BCLEs and the HCLEs were integrated onto the waverider vehicles by matching the local thickness of the leading edge, measured normal to the freestream flow direction and within the osculating plane. The local leading edge thickness was obtained by engineering correlations of the swept stagnation point heating.

The stagnation point heating rate for a swept hemi-cylindrical leading edge, q_{swept}, can be related to that of an unswept leading edge, $q_{unswept}$, using the correlation[34],

$$\frac{q_{swept}}{q_{unswept}} = \left(\cos \lambda_{loc}\right)^{1.1} \quad (1)$$

where λ is the leading edge sweep angle measured from the freestream direction.

The stagnation point heating rates for two hemi-cylindrical leading edges with different leading radii, r_1 and r_2, are related[35] as,

$$\frac{q_{r_2}}{q_{r_1}} = \frac{\sqrt{r_1}}{\sqrt{r_2}} \quad (2)$$

Equations (1) and (2) are assumed to be equally applicable to the optimized BCLEs.

The peak cold wall heating rate data are plotted against Total Height at Mach 5 and 70,000 ft. for the HCLE and BCLE in Figures 28 a) and 28 b), respectively. The predicted heating rates are illustrated with a red line and red "+" symbols. Both leading edge configurations show the characteristic behavior of a $1/\sqrt{L}$ relationship. On each plot a solid black line has been added to illustrate this relationship, using proportionality constants of 77.89 and 70.42 for the HCLE and BCLE, respectively. The agreement is quite good for both leading edge configurations, and similar behavior was found for the other two sets of freestream conditions. These results validate the assumption made in equation (2) that the peak heating is proportional to the reciprocal of the square-root of the Total Height for both leading edge designs.

Renaming the "unswept" conditions as the waverider "centerline" conditions, equations (1) and (2) can be combined to yield an equation for the off-centerline leading edge radius, r_{swept}, that will generate the same heating as the centerline radius, as a function of centerline radius, r_{CL}, and local leading edge sweep, λ_{loc},

$$r_{swept} = r_{CL}\left(\cos \lambda_{loc}\right)^{2.2}$$

Along the span of each of the three vehicles, the local leading edge thickness was scaled such that the Total Height was twice the r_{swept} value. This process produced a non-uniform distance of sharp-edged leading edge that was removed. The result was that the planform of the vehicles were changed. These planform changes varied by vehicle and were smallest for the Mach 10 Hypersonic Cruise Vehicle, and greatest for the Mach 20 Boost-Glide Vehicle. No attempt was made to maintain the original planform. The planform areas calculated with the original sharp-edged geometries were used as the vehicle reference areas for the quantification of the aerodynamics. With the process defined to scale the leading edges from the unswept centerline to the waverider's span, integration with the vehicle could be conducted.

E. Vehicle-Level Aerodynamic Impacts

The sharp leading edged vehicle aerodynamics were calculated using Supersonic/Hypersonic Arbitrary Body Program[36] with Van Dyke's Unified small-disturbance theory[37] impact method for compression surfaces and Prandtl-Meyer expansion theory for the expansion surfaces. The three vehicles were evaluated at zero angle-of-attack (i.e. the orientation at which the waveriders were constructed) and at the design freestream conditions. For the ABM and HCV waveriders, no propulsive surfaces (i.e. engine interior, cowl outer mold line, nozzle, and no propulsion-induced effects on the fore-body or aft-body) were included in the aerodynamic quantification. For the BGV, the base drag was modeled with a local pressure coefficient, $C_p = -1/M^2$.

For each of the three vehicles, the drag contributed by the portions of the sharp leading edge replaced by either the BCLE or the HCLE were removed from the aerodynamic data and the pressure drag from the finite leading edge added. Due to the bluntness of the finite leading edge shapes, Modified Newtonian Flow Model was used to calculate the pressure distributions using a coefficient of 1.83. Due to the large length Reynolds numbers for each of these vehicles, a turbulent boundary layer was expected over most of the acreage areas. The viscous skin friction drag was calculated assuming a turbulent boundary layer everywhere downstream of the leading edge with Van Driest Method II (VDII) employed to calculate the local skin friction coefficient. Although localized regions of laminar flow may be present immediately downstream of the leading edges, the turbulent boundary layer assumption was uniformly applied to produce a higher viscous drag contribution, thereby producing a conservative estimate of any favorable impacts from the leading edge pressure drag reductions on the vehicle. As mentioned earlier, no viscous drag on the blunt leading edges was included in the drag build-up.

The aerodynamic drag reductions when using smaller scaled BCLE, relative to the originally scaled HCLE performance, for the three hypersonic vehicles are listed in Table 1.

Mission	Freestream Mach Number	Optimized BCLE Drag Reduction versus HCLE without Fins (%)	Optimized BCLE Drag Reduction versus HCLE with Fins (%)
Air-Breathing Missile	5	3.2	6.2
Hypersonic Cruise Vehicle	10	~0	~0
Boost-Glide Vehicle	20	<1%	N/A

Table 1 – Vehicle Aerodynamic Drag Differences Between Leading Edge Geometries.

Differences in the aerodynamic lift produced were assumed to be negligible between the HCLE and the BCLEs, and were not quantified. This is a conservative assumption since the BCLE geometry has a wedge appearance and would be expected to generate a small amount of lift. Within the limits of these assumptions, the drag reductions quoted in Table 1 translate directly into increases in the lift-to-drag ratio at the design conditions.

For the Mach 5 Air-Breathing Missile the drag reduction from just modifying the forebody leading edge was 3.2% This drag reduction would increase to 6.2% when the four fins were also modified using the same process described earlier. The fins have significantly more leading edge length, but are swept back at fairly large angles. This reduces the drag benefit potential from the optimized leading edges. By looking at only the pressure drag comparison on the waverider leading edge only case, a 9.1% drag reduction was observed.

For the Mach 10 Hypersonic Cruise Vehicle, the drag reduction was negligible when just the forebody's leading edge was modified and when both the forebody and the fins' leading edges were modified. For such a large vehicle, the leading edge geometry is a small player in the pressure drag. Therefore, one could expect the optimized BCLE to have a small impact on overall vehicle aerodynamic performance.

For the Mach 20 Boost-Glide Vehicle, the drag reduction was less than 1%. This vehicle did not have fins, and therefore no further drag reductions were possible. Larger reductions would be expected as the physical scale of the leading edge is increased. Such an increase would be expected to occur when choosing a lower TPS maximum temperature. The current choice of 6000°F greatly reduced the leading edge size on the BGV studied, and minimized the drag impacts.

When limiting consideration to only the pressure drag, the best current results (9.1%) approach the level of peak drag reduction predicted in the qualitative analysis presented in Reference 19 (13%) for laminar flow leading edges. Both studies indicate potential drag advantages, when using optimized leading edge shapes that exploit the maximum temperature capabilities of a given TPS material, that vary significantly with configuration and conditions. The greater impact predicted from qualitative analysis when assuming turbulent flow conditions on the leading edges, remains to be quantified at the vehicle level.

V. Conclusions

Waverider design approaches generate vehicles that have sharp leading edges. Manufacturing and/or thermal limits usually require that a finite radius be employed at the leading edge. In the current study, Bezier Curve leading

American Institute of Aeronautics and Astronautics

edges have been optimized for use on waverider-based vehicles designed for three typical hypersonic applications: a Mach 5 Air-Breathing Missile, a Mach 10 Hypersonic Cruise Vehicle, and a Mach 20 Boost-Glide Vehicle. The optimization process employed a Particle Swarm Optimizer and used the peak laminar heating rate as the cost function to be minimized. For each vehicle, the optimized leading edges were considerably blunter than hemi-cylindrical shapes. This bluntness reduced the heating around the stagnation point and increased the heating away from the stagnation point, resulting in a more uniform distribution of peak surface temperature and a more effective utilization of the leading edge material temperature limits.

Both Reynolds number and Mach number sensitivities for the Bezier Curve leading edges were examined. A comparison of the three original optimized geometries indicates a very small sensitivity to freestream Mach number. This current observation is in agreement with previous work. Additional optimizations were performed over a two-orders-of-magnitude range of Reynolds numbers. For these three nominal sets of conditions and over these Reynolds numbers ranges, the optimized shapes were found to be quite insensitive to Reynolds number.

Empirical relationships were employed to scale the optimized leading edges, and similar conventional hemi-cylindrical leading edge geometries, to account for geometric scaling and leading edge sweep. The resulting leading edge geometries were incorporated onto the waveriders, while holding the leading edge material radiative equilibrium temperature as a constant between leading edge configurations. The resulting integrated vehicle aerodynamic performance has been quantified and compared between optimized Bezier Curve leading edges and hemi-cylindrical configurations. For these three cases vehicle-level drag reductions of 0-6.2% were observed when using Bezier Curve leading edges versus the hemi-cylindrical leading edges, with the greatest drag reduction appearing with the Mach 5 Missile. These aerodynamic results were obtained from using the Van Dyke Unified Theory and the Modified Newtonian impact methods for the pressure drag on the waveriders and leading edges, respectively, and using the Van Driest II turbulent model for the viscous drag for the acreage area.

References

[1]Eggers, A.J., Resknikoff, M.M., Dennis, D., H., "Bodies of revolution having minimum drag at high supersonic airspeeds," NACA Report #1306, 1957.

[2]Eggers, A.J., Ashley, H., Springer, G.S., Bowles, J.V., and Ardema, M.D., "Hypersonic Waverider Configuration from the 1950's to the 1990's," AIAA Paper 93-0774, Reno, NV, 1993.

[3]Bowcutt, K.G., Anderson, J.D., and Capriotti, D., "Viscous Optimized Hypersonic Waveriders," AIAA Paper 87-0272, Reno, NV, 1987.

[4]Corda, S., and Anderson, J.D., "Viscous Optimized Hypersonic Waveriders Designed from Axisymmetric Flow fields," AIAA Paper 88-0369, Reno, NV, 1988.

[5]Center, K.B., Sobieczky, H. and Dougherty, F.C., "Interactive Design of Hypersonic Waverider Geometries," AIAA Paper 91-1697, Honolulu, HI, June 1991.

[6]Mill, R.W., Argrow, B.M., Center, K.B., Brauckmann, G.J., and Rhode, M.N., "Experimental Verification of the Osculating Cones Method for Two Waverider Forebodies At Mach 4 and 6," AIAA Paper 98-0682, Reno, NV, 1998.

[7]Jones, K.D., and Center, K.B., "Waverider Design Methods for Non-Conical Shock Geometries," AIAA Paper 2002-3204, St. Louis, MO, 2002.

[8]Rodi, P.E., "The Osculating Flowfield Method of Waverider Geometry Generation,"AIAA Paper 2005-0511, Reno, NV, 2005.

[9]Rodi, P.E., and Genovesi, D., "Engineering-Based Performance Comparisons Between Osculating Cone and Osculating Flowfield Waveriders," AIAA Paper 2007-4344, Miami, FL, 2007.

[10]Rodi, P.E., "Geometrical Relationships for Osculating Cones and Osculating Flowfield Waveriders," AIAA Paper 2011-1188, Orlando, FL, 2011.

[11]Mason, W.H., and Less, J., "Aerodynamically Blunt and Sharp Bodies," AIAA Journal of Spacecraft and Rockets, vol. 31, May-June 1994, pp. 378-382.

[12]O'Brien, T.F., Lewis, M.J., "Power Law Leading Edges for Waveriders Designed with Shock Attachment," AIAA Paper 1998-0600, Reno, NV, 1998.

[13]O'Brien, T.F., Lewis, M.J., "Power Law Shapes for Leading-Edge Blunting with Minimal Shock Standoff," *AIAA Journal of Spacecraft and Rockets*, Vol., 36, No. 5, September-October 1999, pp. 653-658.

[14]Santos, W.F.N., "Bluntness Effects on Lift-to-Drag Ratio of Leading Edges for Hypersonic Waverider Configurations," AIAA Journal of Spacecraft and Rockets, Volume 46, Number 2, March-April 2009.

[15]Santos, W.F.N., and Lewis, M.J., "Aerothermodynamic Performance Analysis of Hypersonic Flow on Power Law Leading Edges," AIAA Journal of Spacecraft and Rockets, Vol. 42, No. 4, July-August 2005, pp588-597.

[16]Vanmol, D.O., and Anderson, Jr., J.D., "Heat Transfer Characteristics of Hypersonic Waveriders with an Emphasis on Leading Edge Effects, " AIAA Paper 1992-2920, July, 1992.

[17]Rodi, P.E., "Optimization of Bezier Curves for High Speed Leading Edge Geometries," AIAA Paper 2013-1004, January 2013.

[18]Cui, K., and Hu, S.-C., "Shape Design to Minimize the Peak Heat-Flux of Blunt Leading-Edge," AIAA Paper 2013-0233, January 2013.

[19]Rodi, P.E., "Integration of Optimized Leading Edges Onto Waverider Configurations," 2014 AIAA Houston Section Annual Technical Symposium, May 9th, 2014.

[20]Kennedy, J., and Eberhart, R., "Particle Swarm Optimization," in *Proceedings of IEEE International Conference on Neural Networks,* pp. 1942-1948, 1995.

[21]Sam, "Another Particle Swarm Toolbox," Mathworks User Community, http://www.mathworks.com/matlabcentral/fileexchange/25986-another-particle-swarm-toolbox.

[22]Sohn, M.H., and Lee, K.J., "Bezier Curve Application in the Shape Optimization of Transonic Airfoils," AIAA Paper 2000-4523, August, 2000.

[23]Samareh, J.A., "Survey of Shape Parameterization Techniques for High-Fidelity Multidisciplinary Shape Optimization," *AIAA Journal*, Vol., 39, No. 5, May 2001, pp. 877-884.

[24]Eyi, S., and Yumusak, M., "Design Optimization in Hypersonic Flows," AIAA Paper 2012-5827, Tours, France, September 2012.

[25]Kays, W.M., Convective Heat and Mass Transfer, McGraw-Hill, New York, 1966, Chapters 10, 11, and 13.

[26]Hank, J.M., Murphy, J.S., and Mutzman, R.C., "The X-51A Scramjet Engine Flight Demonstration Program," AIAA Paper 2008-2540, April 2008.

[27]Heiser, W.H., Pratt, D.T., Daley, D.H., and Menta, U.B., *Hypersonic Airbreathing Propulsion*, AIAA Education Series, American Institute of Aeronautics and Astronautics, Washington, D.C., 1994.

[28]Olds, J.R., and Budianto, I.A., "Constant Dynamic Pressure Trajectory Simulation with POST," AIAA Paper 1998-0302, January 1998.

[29]http://www.darpa.mil/Our_Work/TTO/Falcon_HTV-2_Three_Key_Technical_Challenges.aspx

[30]Paul, A., Jayaseelan, D.D., Venugopal, S., Zapata-Solvas, E., Binner, J., Vaidhyanathan, B., Heaton, A., Brown, P., and Lee, W.E., "UHTC composite for hypersonic applications," American Ceramic Society Bulletin, Vol. 91, No. 1, pp 22-28.

[31]Williams, S.D., and Curry, D.M., "Thermal Protection Materials," NASA RP-1289, 1992.

[32]Loehman, R., Corral, E., Dumm, H.P., Kotula, P., and Tandon, R., "Ultra High Temperature Ceramics for Hypersonic Vehicle Applications," Sandia Report SAND 2006-2925, June 2006.

[33]Wuchina, E., Opila, E., Fahrenholtz, W., and Talmy, I., "UHTCs: Ultra-High Temperature Ceramic Materials for Extreme Environment Applications," The Electrochemical Society *Interface*, Winter 2007.

[34]Hayes, J.R., and Neumann, R.D., "Introduction to the Aerodynamic Heating Analysis of Supersonic Missiles," AIAA Progress in Astronautics and Astronautics Volume 142, Edited by Michael r. Mendenhall, 1992.

[35]Bertin, J.J., *Hypersonic Aerothermodynamics*, AIAA Education Series, New York, New York, 1993.

[36]Burns, K.A., Deters, K.J., Haley, C.P., and Kihlken, T.A., "Viscous Effects on Complex Configurations – Software User's Manual," WL-TR-95-3060, August 1995.

[37]Van Dyke, M., "A Study of Hypersonic Small-Disturbance Theory," NACA Report 1194, March 1954.

Figures
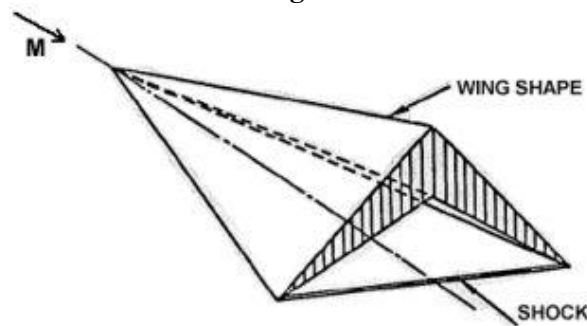
Figure 1 – A Caret Waverider Geometry, from Reference 2.

11
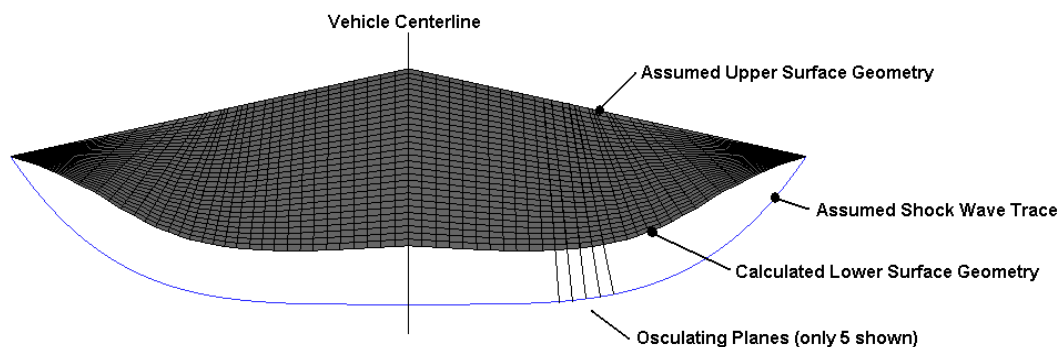
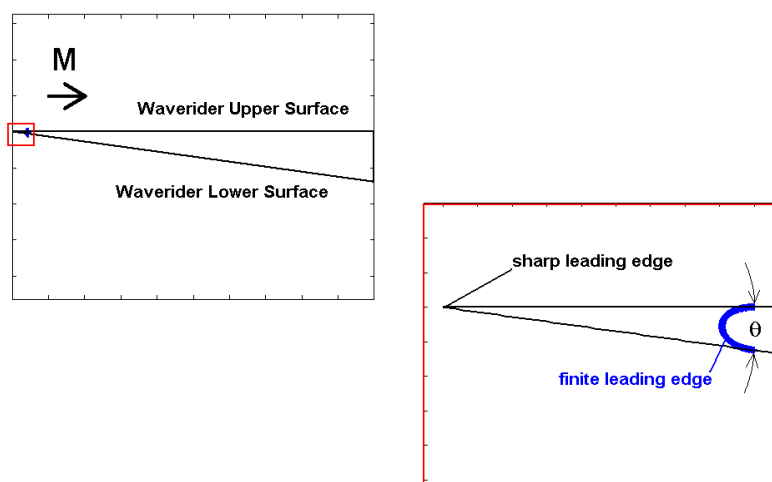**Figure 2 – Baseplane of an Osculating Flowfield Waverider, from Reference 10.**

Figure 3 – One Waverider Osculating Plane,
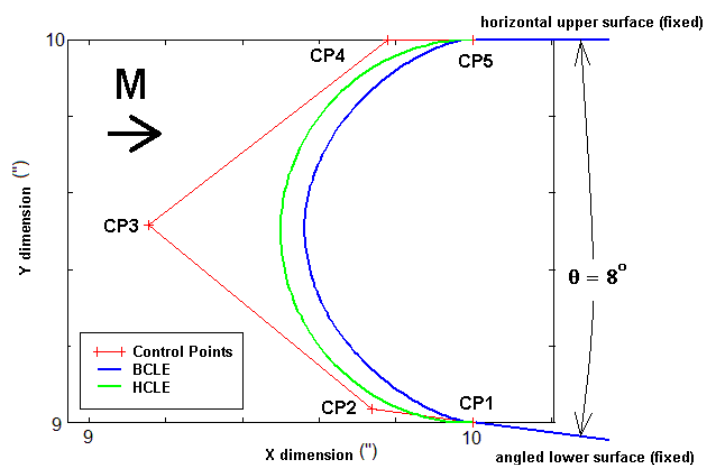**Illustrating Sharp and Finite Leading Edges.**

Figure 4 – A Fourth-Order Bezier Curve Leading Edge Using Five Control Points,
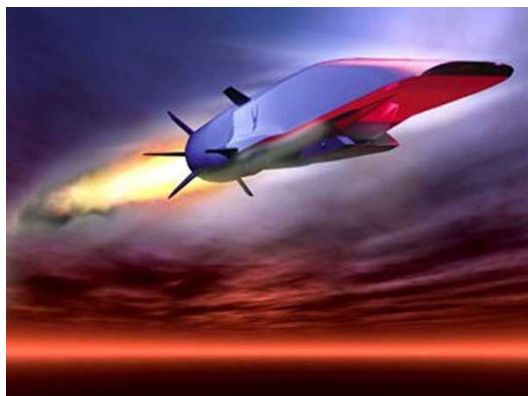**for an 8° Wedge Angle.**

12
American Institute of Aeronautics and Astronautics

Figure 5 – The X-51A Air-Breathing Hypersonic Vehicle.
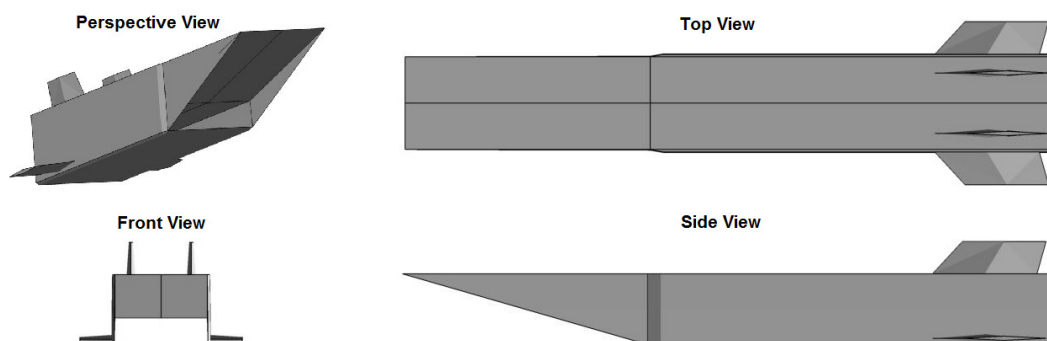
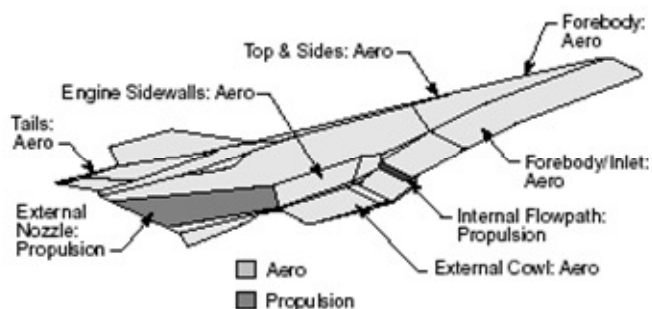**Figure 6 – A Waverider Designed for the Mach 5 Air-Breathing Vehicle Conditions.**

Figure 7 – Force Accounting Convention For Both Air-Breathing Vehicles.

Figure 8 – A Hypersonic Cruise Vehicle Design from DARPA's Falcon Program.
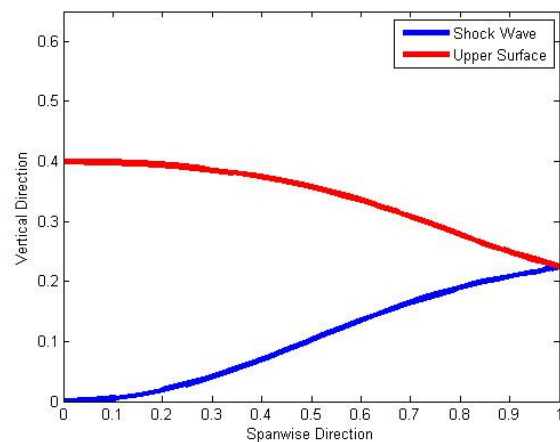
Figure 9 – Shock Wave and Upper Surface Traces for the Mach 10 Hypersonic Cruise Vehicle Waverider Configuration.
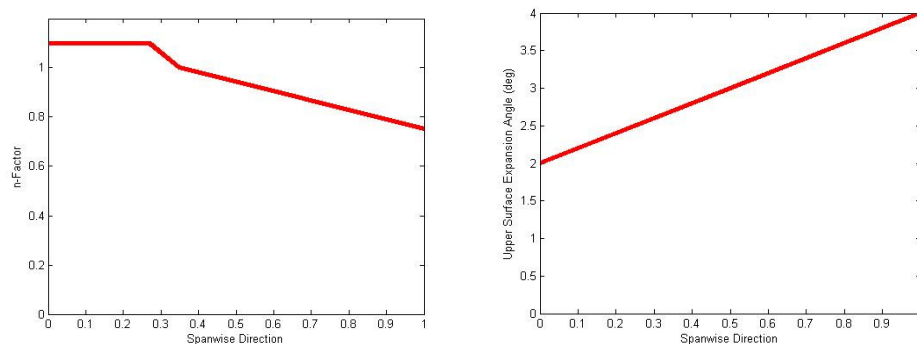
a) n-Factor   **b) Upper Surface Expansion**

Figure 10 – n-Factor and Upper Surface Expansion for the Mach 10 Hypersonic Cruise Vehicle Waverider Configuration.
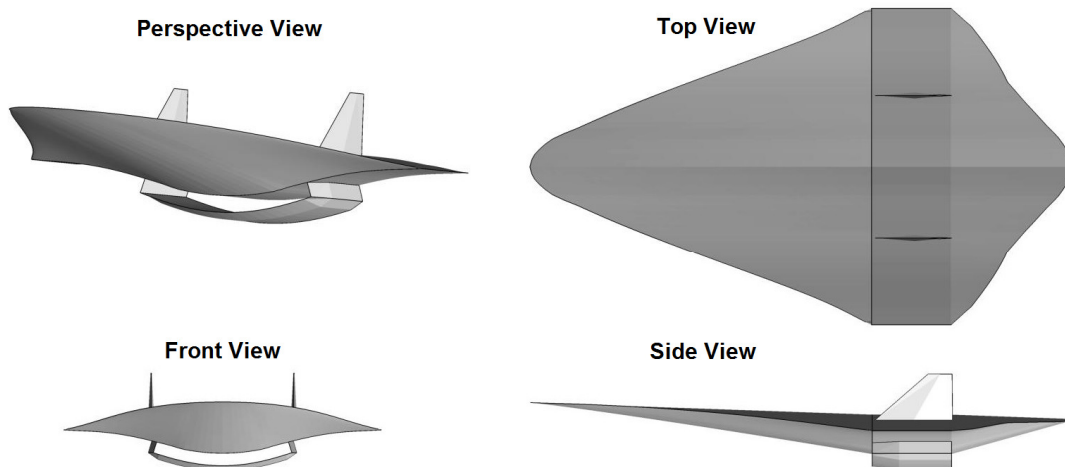
Figure 11 – A Waverider Designed for the Mach 10 Hypersonic Cruise Vehicle Conditions.

14
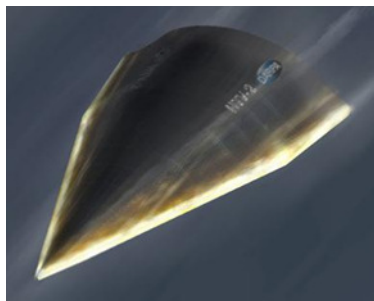
Figure 12 – Artists Impression of the HTV-2 In Flight.
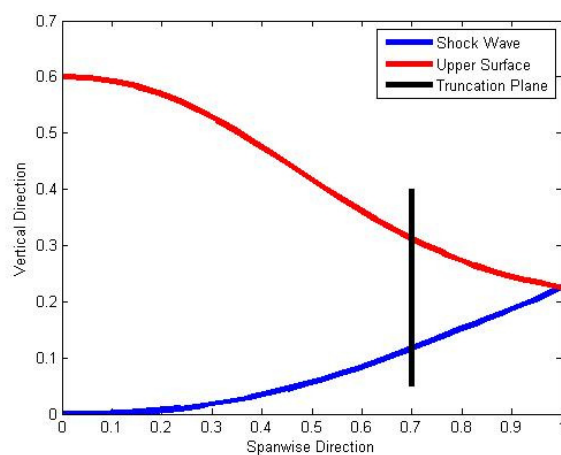
Figure 13 – Shock Wave and Upper Surface Traces for the Mach 20 Boost-Glide Vehicle Waverider Configuration.
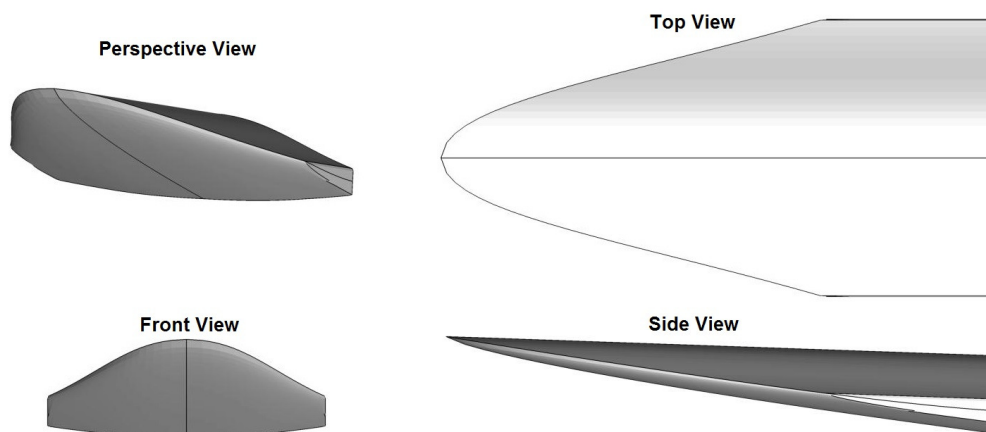
Figure 14 – A Waverider Designed for the Mach 20 Boost-Glide Conditions.

American Institute of Aeronautics and Astronautics
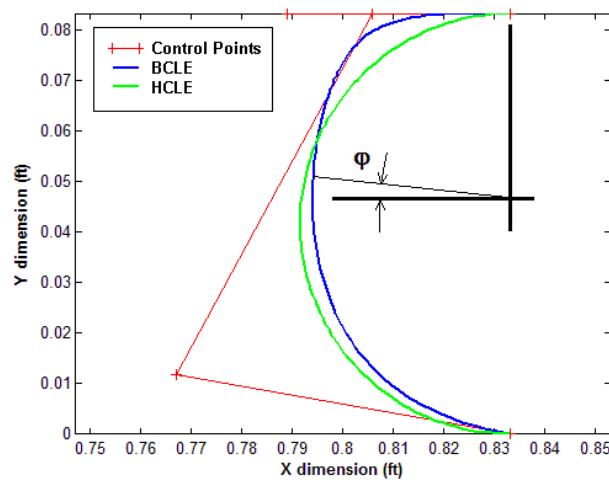
Figure 15 – Bezier Curve Optimized Leading Edge Generated for the θ=10º, Mach 5, h=70,000 feet, with Total Height=1".
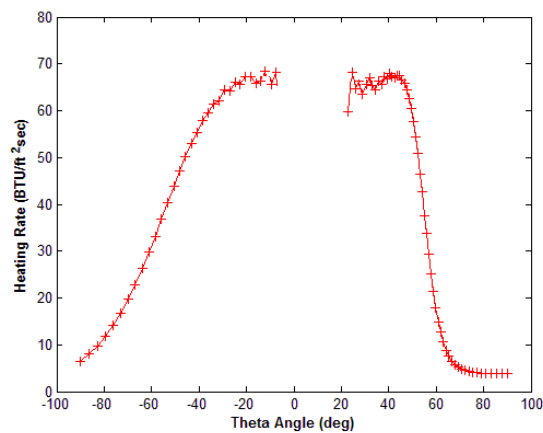
Figure 16 – Laminar Heating Distribution for the Bezier Curve Optimized Leading Edge Generated for θ =10º, Mach 5, h=70,000 feet, with Total Height=1".
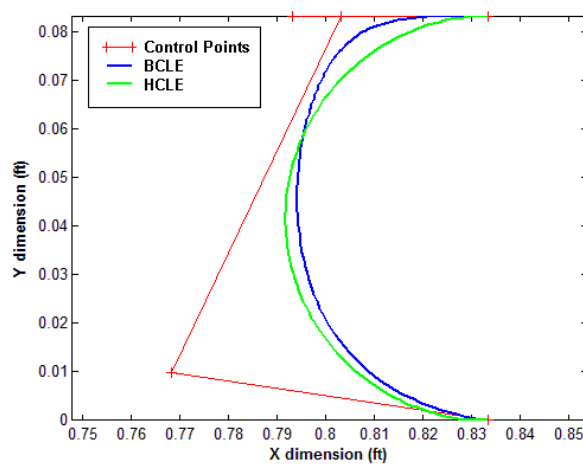
Figure 17 – Bezier Curve Optimized Leading Edge Generated for the θ_W =8.5º, Mach 10, h=95,100 feet, with Total Height=1".
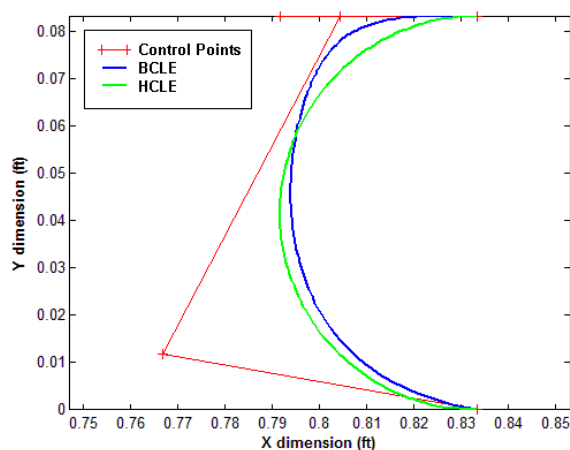
Figure 18 – Bezier Curve Optimized Leading Edge Generated for the θ =10º, Mach 20 at h=120,000 feet, with Total Height=1".
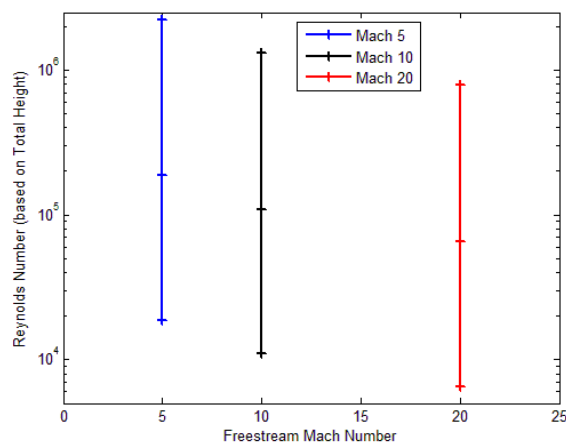
Figure 19 – Reynolds Number vs. Mach Number for the Nine Bezier Curve Leading Edge Optimizations Performed.
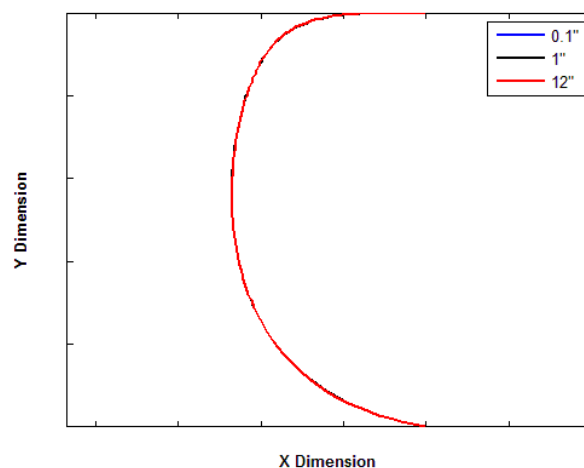
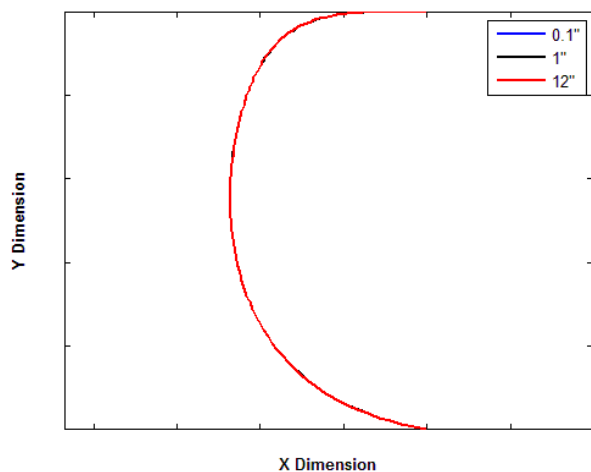**Figure 20– Reynolds Number Effects on Optimized Leading Edge Geometries at Mach 5, θ =10º, and h=70,000 feet.**

American Institute of Aeronautics and Astronautics
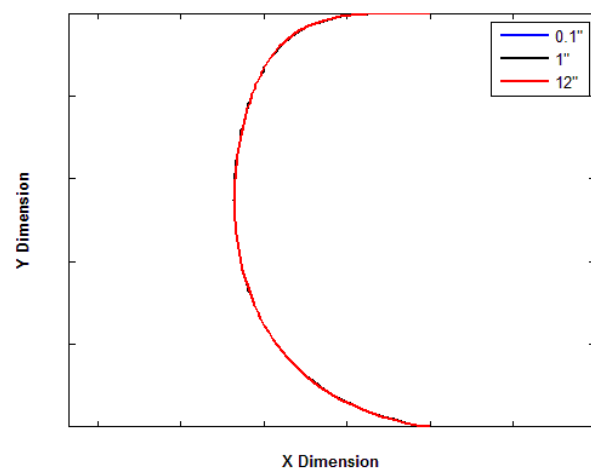
Figure 21 – Reynolds Number Effects on Optimized Leading Edge Geometries at Mach 10, θ =8.5º, and h=95,100 feet.

Figure 22 – Reynolds Number Effects on Optimized Leading Edge Geometries at Mach 20, θ =10º, and h=120,000 feet.
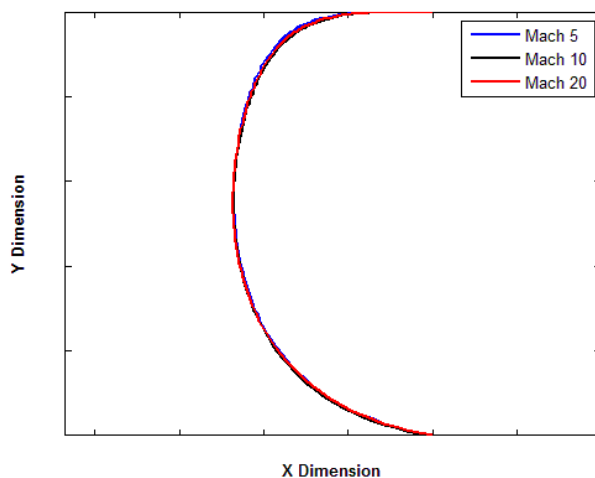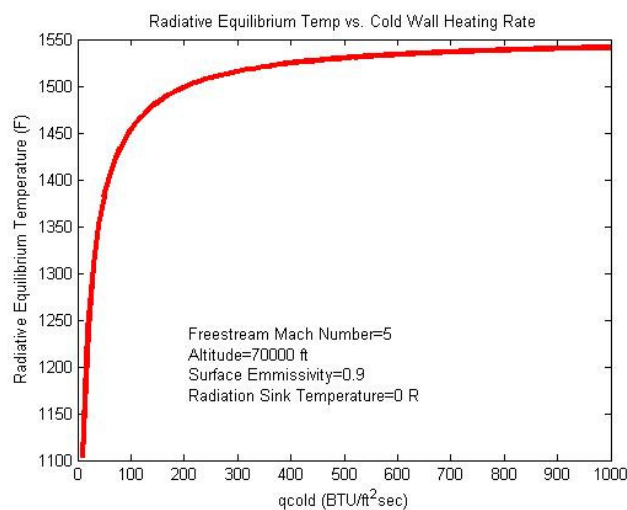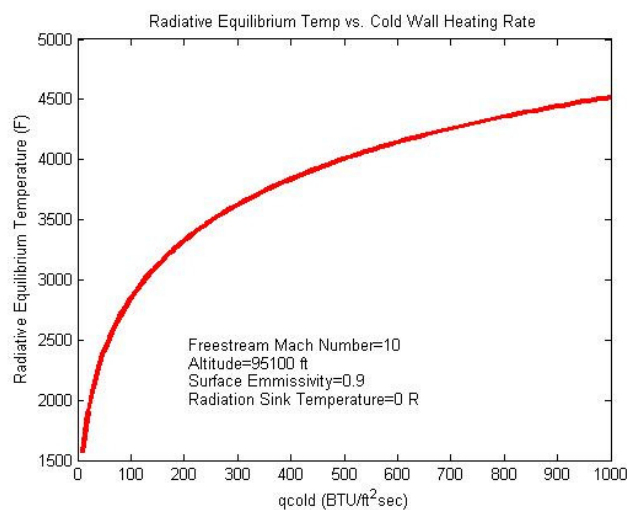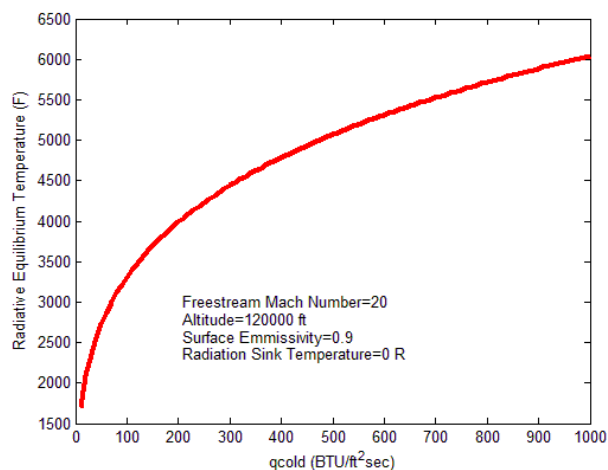

Figure 23 – Mach Number Effects on Optimized Leading Edge Geometries Generated at the Nominal Conditions and using a Total Height of 1".
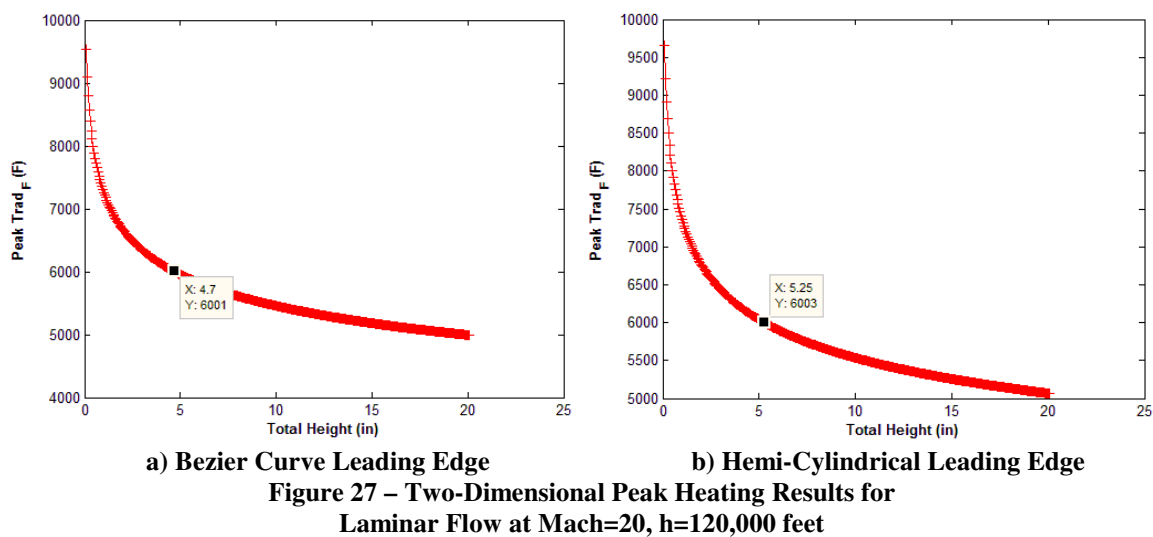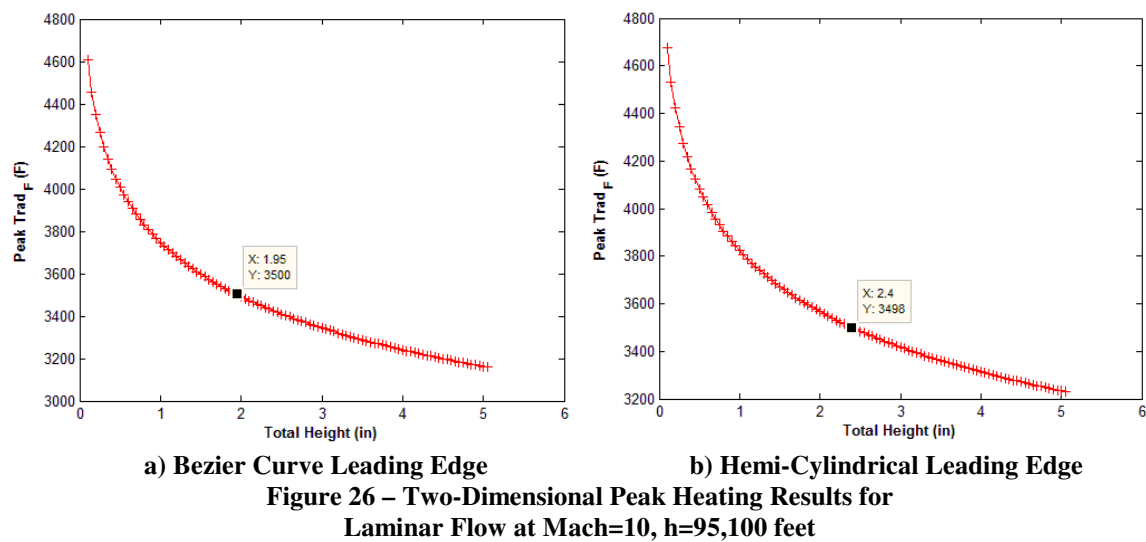
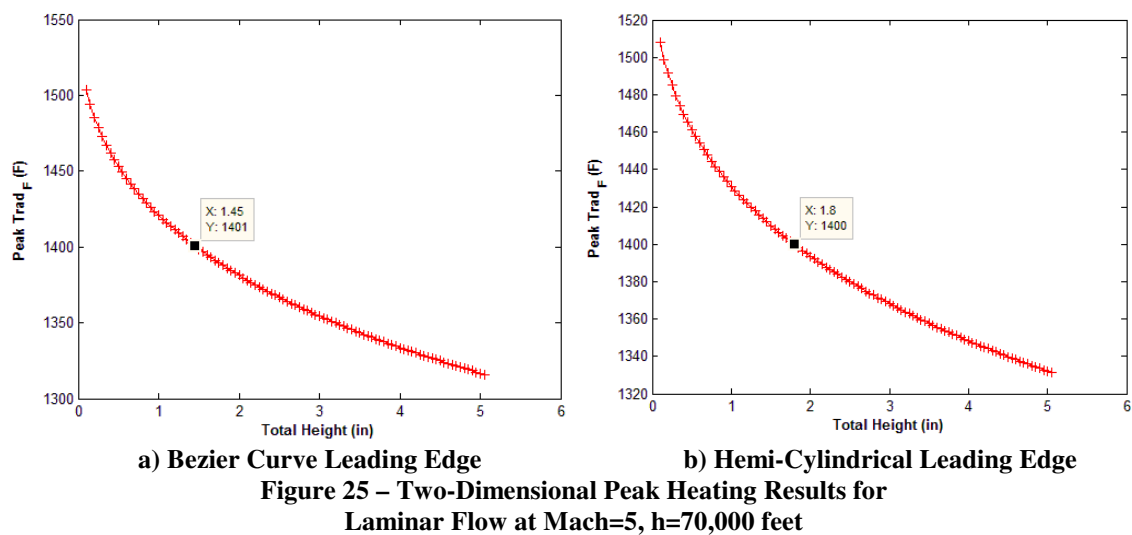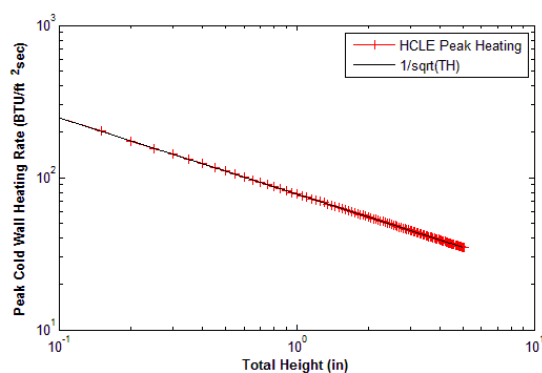**a) Mach=5 and Altitude=70,000 feet**

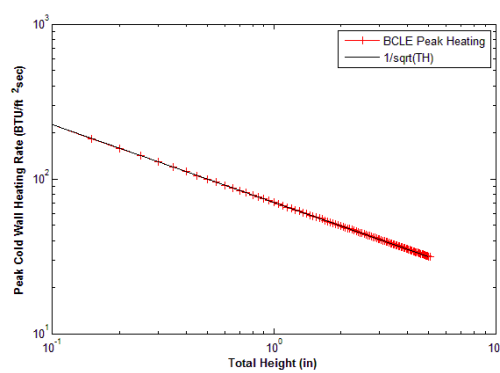**b) Mach=10 and Altitude=95,100 feet**

c) Mach=20 and Altitude=120,000 feet
Figure 24 – Radiative Equilibrium Temperatures vs. Cold Wall Heating Rate
for the Three Mach/Altitude Cases.

American Institute of Aeronautics and Astronautics

a) Bezier Curve Leading Edge   **b) Hemi-Cylindrical Leading Edge**
Figure 25 – Two-Dimensional Peak Heating Results for
Laminar Flow at Mach=5, h=70,000 feet

a) Bezier Curve Leading Edge   **b) Hemi-Cylindrical Leading Edge**
Figure 26 – Two-Dimensional Peak Heating Results for
Laminar Flow at Mach=10, h=95,100 feet

a) Bezier Curve Leading Edge   **b) Hemi-Cylindrical Leading Edge**
Figure 27 – Two-Dimensional Peak Heating Results for
Laminar Flow at Mach=20, h=120,000 feet

American Institute of Aeronautics and Astronautics

a) Hemi-Cylindrical Leading Edge **b) Bezier Curve Leading Edge**
Figure 28 – Peak Cold Wall Heating Rate vs. Total Height at,
Mach=5, h=70,000 feet

American Institute of Aeronautics and Astronautics